EUROPEAN FUSION DEVELOPMENT AGREEMENT

EFDA–JET–PR(02)17

W. Fundamenski and S. Sipila

Boundary Plasma Energy Transport in JET ELMy H-modes

Boundary Plasma Energy Transport in JET ELMy H-modes

W. Fundamenski and S. Sipila[1]
and contributors to the EFDA-JET workprogramme*

Euratom/UKAEA Fusion Association, Culham Science Centre, Abingdon, Oxon, UK
[1]Helsinki University of Technology, Tekes-Euratom Assoc., PO Box 2200, FIN-02015 HUT, Finland
** See annex of J. Pamela et al, "Overview of Recent JET Results and Future Perspectives", Fusion Energy 2000 (Proc. 18th Int. Conf. Sorrento, 2000), IAEA, Vienna (2001).*

Preprint of Paper to be submitted for publication in
Physics Review Letters

ABSTRACT

The radial extent of a magnetised boundary plasma, or Scrape-Off-Layer (SOL), is determined by competition between transport processes parallel (||) and perpendicular ($\perp$) to the magnetic field B [1]. Whereas most aspects of || transport are well understood, $\perp$ transport is generally anomalous, determined largely by turbulent processes [1], a situation common to many areas of plasma physics, eg. planetary magnetospheres, solar corona, wind, prominences and flares, magnetic accretion jets and many industrial plasmas. In nuclear fusion devices, the radial extent of the SOL determines the peak heat flux on the divertor tiles which poses a key constraint on the design and successful operation of a next-step tokamak, such as ITER [2]. In order to improve our predictive capability, physical understanding of the underlying $\perp$ transport mechanisms is essential, especially in the reference regime of ITER, the so called ELMy H-mode [3]. With this aim, a series of experiments were carried out on JET in which power deposition widths λ_q were measured in several D and He plasmas, including scans in toroidal B_ϕ and poloidal B_θ fields, neutral beam power PNB and line average density $<n_e>$. The aim of this letter is the interpretation of the above experiments, specifically the comparison of experimental q with predictions of ~ thirty candidate models of $\perp$ energy transport.

EXPERIMENTAL RESULTS.

Power widths λ_q were measured for twenty discharges in total (14 D, 6 He). The nine discharges (3 D, 6 He) selected for the present study based on lack of B_ϕ or B_θ variation in the D data [4] and quality of diagnostic data are listed in Table 1. They represent the only data set of its kind on a large tokamak [5]. All plasmas have identical shape and the direction of toroidal field such that B x ∇B points towards the divertor. The selected set contains several He H-modes with variation of and the magnetic safety factor $q_{95} \sim aB_\phi/RB_\theta$, as well as two D H-modes and three L-modes. The line-average density varies by a factor of two, which spans the Greenwald fraction f_{GW} from ~0.3 in L-mode, through ~0.6 in D H-modes, up to the ITER relevant values of 0.8-1.0 in He H-modes.

ELM-averaged power deposition profiles were obtained for each of the above discharges using the swept strike-point Thermo-Couple (TC) technique [4,6], which agrees closely with the Infra-Red (IR) diagnostic [7]. Since ELMs are responsible for only ~20-30% of the energy reaching the divertor targets [8], these profiles are dominated by inter-ELM energy transport. In addition, electron power profiles were measured using the divertor Langmuir Probes (LP) [6,9]. The profiles are parametrized in terms of two variables: peak heat flux q_0 and the integral width, defined as $\lambda_q \equiv \int q dr / q_0$. The results for the outer target are summarised in Table 1 (q_0^{inner} is up to five times smaller). All heat fluxes are expressed as wall loads, i.e. per unit area of the divertor target; heat fluxes || to the magnetic field are related to target fluxes by $q_{||}/q_t \sim 1/\sin\theta_\perp$, where $\theta_\perp \sim 4\text{-}5^o$ is the field line angle normal to the target. Profile widths are mapped from the target to the outer mid-plane (omp) or upstream location using $\lambda_q[\text{omp}] = \lambda_q[z]/\Phi$, where $\Phi \sim 4$ is the flux expansion factor obtained using EFIT reconstruction.

The ion contribution to q_0 may be estimated as the difference between the TC and LP measurements. Ions dominate q_0 in D H-modes, which is evidently not the case for helium. This fact is largely explained by examining ion υ^*_i and electron υ^*_e collisionalities, defined as the ratio of upstream-to-target connection length $L_\parallel \propto Rq_{95}$ to upstream α-β mean-free-path with $\alpha,\beta,\in \{e,i\}$: $\upsilon^*_{\alpha\beta} \equiv L_\parallel/\lambda_{\alpha\beta} = L_\parallel(3T_\alpha/m_\alpha)^{-1/2}\,\upsilon_{\alpha\beta}$; note that, $\upsilon_{ee}:\upsilon_{ii}:\upsilon_{ie} = 1:Z^3\,\vartheta^{-3/2}\,(m_e/m_i)^{1/2}:Z^2\,m_e/m_i$ (where $\vartheta\,T_i/T_e$) are ordered by $(m_e/m_i)^{1/2} \ll 1$, while $\lambda_{ee}:\lambda_{ii}:\lambda_{ie} = \vartheta^2 Z^{-3}:Z^{-1}:1$ are of the same order of magnitude [10]. These have been calculated using modified two-point model estimates [11,12] of upstream separatrix temperature $T_{e,u}$ and density $n_{e,u}$ (assuming $\vartheta_u = 2$), based on target LP measurements of $T_{e,t}$ and $n_{e,t}$, Table 1. It is clear that in D H-modes ions are only marginally collisional ($\upsilon^*_i < 3$), whereas in He plasmas $\upsilon^*_i \cong \upsilon^*_{ei} \sim 30$, which precludes Ion Orbit Loss (IOL) and implies strong coupling between ion and electron channels (hence $q_0^{TC} \sim q_0^{LP}$ in helium).

Table 1 also gives the estimate of the power entering the SOL ($P_{SOL} \sim P_\Omega + P_{NB} - P_{rad}$) and the total power deposited on the outer target (TC). The in-out power asymmetry is nearly constant for all the discharges, P_t outer $/P_{SOL} \sim 0.6$-0.7. This is consistent with previous D results where in-out asymmetry was shown to be a function of only the B x∇B direction [8]. The fact that P_{SOL} / P_{NB} is greater in helium reflects the increase in ohmic heating power P_Ω with plasma resistivity,$\eta_\parallel \propto Z$.

STATISTICAL ANALYSIS.

Standard regression analysis was performed on TC and LP widths with respect to ion mass A and charge Z, B_f, q_{95}, P_t and $n_{e,u}$. Since A/Z=2 for both D^+ and He^{++}, one of these variables is redundant in the regression; we shall denote this by writing A(Z). The choice of P_t and $n_{e,u}$ as the two plasma variables was dictated by three factors:

a) continuity with literature [3],
b) accuracy of estimates,
c) comparison with theory.

Whereas P_t was directly measured, upstream $(T_i, T_e, n_e)_u$ are calculated based on target quantities $(T_e, n_e)_t$ and the diagnostically unavailable $\vartheta = T_i/T_e$ ratio. Comparison with theory complicates the matter further, since most models depend on both T_i and T_e, the former of which is unknown. In what follows, we present regression with respect to *all* variables but exclude the scaling with *plasma* variables (P_t, $n_{e,u}$) from the comparison with theory (this does not alter the conclusions of the study).

The regression was performed on five sets of discharges: all D + He; selected data (Table 1); H-mode only; D only and He only. The resulting scalings are summarized in Table 2; they may be approximated as $\lambda_q^{TC} \propto A(Z) q_{95}^{3/4} B_\phi^{-1} P_t^{-0.4} n_{e,u}^{0.15}$. Since the A(Z), B_ϕ and q_{95} exponents show only a mild variation between the data sets, we incur only a small error by a particular choice of data set (e.g. the exclusion L-mode shots). Consequently, the first entry in Table 2 was chosen as the reference experimental scaling to be compared with theory.

The LP width is roughly proportional and slightly larger than its TC equivalent, $\lambda_q^{LP}/\lambda_q^{TC} \sim 1.25\pm0.23$. The two widths exhibit similar scalings, aside from a stronger density and weaker power dependence in case of λ_q^{LP}. However, the LP width is less well correlated with the regression variables, as indicated by the regression error, Table 2. This error may be reduced by including the effect of υ^*_{ie}, which suggests that a large fraction of power is coupled to the electrons from the ion channel. In what follows, we restrict our analysis to λ_q^{TC} only.

THEROETICAL DERIVATION OF SOL WIDTHS.

Local power balance in the SOL may be written as $\nabla_{||}q_{||\alpha} + \nabla_{\perp}q_{\perp\alpha} = S_{q,\alpha}$, where $q_{||\alpha} = {}^1/_2(m_\alpha v_\alpha{}^2 + 5T_\alpha)n_\alpha v_{||\alpha} - n_\alpha\chi_{||\alpha}\nabla_{||}T_\alpha$ and $q_{\perp\alpha} = -n_\alpha\chi_{\perp\alpha}\nabla_{\perp}T_\alpha$ are the || and $\perp$ energy fluxes for species $\propto \in \{e,i\}$, $\chi_{||\alpha} \propto T_\alpha\,\tau_\alpha/m_\alpha$ and – are the || and heat diffusivities, and Sq, is the net energy source [1]. The above may be simplified by replacing the || and $\perp$ gradients by inverse lengths $1/L_{||}$ and $1/\lambda_{q\alpha}$, where $\lambda_{q\alpha}$ is the power e-folding length in the SOL. This yields an expression for $\lambda_{q\alpha} \sim \{n_\perp T_\alpha\chi_{\perp\alpha}/|q_{||\alpha}/L_{||} - S_{q\alpha}|\}^{1/2}$ which scales as $(n_\alpha T_\alpha L_{||}\chi_{\perp\alpha}/q_{||\alpha})^{1/2}$ when either $L_{||}S_{q\alpha} << q_{||\alpha}$ or $L_{||}S_{q\alpha} \propto q_{||\alpha}$. Introducing the convective and conductive times ($\tau_{v\alpha} \sim L_{||}/v_{||\alpha}$, $\tau_{\chi\alpha} \sim L_{||}{}^2/\chi_{||\alpha}$), one can express the condition for || heat transport being dominated by convection as $\Xi \equiv \tau_v/\tau_\chi < 5/2$. We approximate the former as $\tau_v \sim L_{||}/Mc_s$ where $c_s = \{(ZT_e+T_i)/m_i\}^{1/2}$ is the plasma sound speed and $M = v_{||}/c_s$ is the Mach number; over the range $1<Z<2$, c_s scales as $\{Z^\xi/A\}^{1/2}$ with $\xi = 0.6$ for $\vartheta = 1$ and $\xi = 0.42$ for $\vartheta = 2$. The latter becomes $\tau_\chi \sim L_{||}{}^2/\chi_{||e}$ since $\chi_{||e}/\chi_{||i} \sim 35A^{0.5}Z^3\,\vartheta^{-2.5}$, which gives ~ 10 for D^+ and ~ 100 for He^{++} (M~0.5 and ϑ~2 will be assumed henceforth in light of evidence for strong SOL flows and energetic ions in the SOL [7,13]). In the convective regime (< 5/2), the power width becomes $\lambda_{qv,\alpha}, \sim (\chi_{\perp\alpha}L_{||}/c_s)^{1/2}$; in the conductive regime ($\Xi < 5/2$), one obtains $\lambda_{qv,\alpha}, \sim L_{||}(\chi_{\perp\alpha}/\chi_{||e})^{1/2}\,(T_\alpha/T_e)^{1/2}$. On the basis of Ξ evaluated at both the upstream and target locations for all discharges of Table 1 ($\Xi_u \sim 10$, $\Xi_t \sim 1$), we expect conduction to dominate in the upstream SOL ($q_{||} \sim n_e\chi_{||e}\nabla_{||}\,T_e$) and convection in the divertor region ($q_{||\alpha} \sim 2.5T_\alpha n_\alpha Mc_s$). Both expressions for λ_q are thus relevant for the present study.

MODELS OF $\perp$ ENERGY TRANSPORT.

Following the approach of Connor et al. [14,15], two dozen models for $\perp$ heat diffusivity $\chi_\perp$were considered. Their scaling with A, Z, B_ϕ, $L_{||} \propto Rq_{95}$, λ_q, n_e and T_α is summarised in Table 3. The model notation of [14] was retained, with three notable additions: the classical A1 and neo-classical A2 ion conduction, as well as classical electron conduction A3. For a detailed description of the underlying physics of each model, the reader should consult [14] and the citations contained therein. Also included in Table 3, are scalings of ion toroidal ρ_i(Y1) and poloidal $\rho_{\theta i}$(Y2) gyro-radii, and electron toroidal ρ_e(Z1) and poloidal $\rho_{\theta e}$(Z2) gyro-radii. Finally, the footprint of IOL on the outer target was obtained via numerical simulations of JET plasmas using the ASCOT code [16]. Over thirty simulations were performed with $1.5\ T < B_\phi < 3.5\ T$, $2.6 < q_{95} < 5.2$, $A \le 12$ and $Z \le 2$, to yield the following expression: λ_q^{IOL} [mm-omp] $= 2.2A^{0.35\pm0.03}\,Z^{-0.8\pm0.06}\,B_\phi^{-0.89\pm0.04}\,q_{95}^{0.88\pm0.04}$. Not

surprisingly, the resulting width, denoted by X in Table 3, scales roughly as the poloidal gyro-radius $\rho_{\theta i}$(Y2) ~ banana width, the differences arising mainly from topological effects associated with the X-point. The above models can be categorized into four families of increasing order of complexity: a) Q,$\chi_\perp$= constant; b) X-Z, λ_q~ gyro-radii; c) A, (neo-)classical conduction, d) B-O, anomalous.

COMPARISON WITH EXPERIMENT

In order to compare the predictions of various theoretical models with experimental results, it is necessary to introduce the $\chi_\perp$ scalings of Table 3 into the $\lambda_{q,v}$ and $\lambda_{q,\chi}$, expressions derived previously. For a general scaling $\chi_\perp \propto A^\mu Z^\eta B^\xi L_\parallel{}^\zeta n_e{}^\psi T_\alpha{}^\theta \lambda_q{}^\sigma$ after some simple algebra, one obtains the results $\lambda_q(A^x Z^y B^z L_\parallel{}^w n_e{}^u T_\alpha{}^v)^s$ where x =(μ +0.5)/2, y =(η -0.21)/2, w =(ζ +1)/2, u =(ψ +1)/2, v=(θ-2.5)/2 for $\lambda_{q,v}$; x =μ/2, y = η /2, w = 1+ ζ/2, u = ψ/2, v =(θ -0.5)/2 for $\lambda_{q,\chi}$, and z = ξ/2, s = 1/(1+ σ/2) for both. In what follows, we introduce the following notation: $\perp$ model A with $\parallel$ assumption a will be termed a mechanism and denoted as A:a. As a figure of merit of the comparison we take the RMS difference Δ between the predicted (model) and measured (regression, 1st entry in Table 2) exponents. This quantity Δ is plotted in ascending order for the best ten models assuming $\parallel$ convection, $\lambda_{q,v}$, Fig.1, and $\parallel$ conduction, $\lambda_{q,\chi}$, Fig.2. By far the best match to the experiment is offered by classical ion conduction A1($\Delta_{A1:v}$=0.12, $\Delta_{A1:\chi}$=0.19), followed by resistive MHD (interchange E and drift ballooning turbulence H), classical electron conduction A3, Bohm N, poloidal gyro-radius Z2, endplate MHD (B2, G2), skin depth I and others. Of all the mechanisms, only A1:v agrees with each exponent to within the regression error, Table 2, and only A1 shows significant improvement over the null model Q, the Δ of models B-Z following a trapezoidal distribution about ΔQ ($\Delta_{<B:Z>:v}$~0.70 vs. $\Delta_{Q:v}$~0.73 and $\Delta_{<B:Z>:\chi}$~0.74 vs. $\Delta_{Q:\chi}$~0.79). The breakdown of Δ into primary components, reveals that over models B to Z, Δ_{AZ} is by far the largest source of discrepancy. Nearly all models under-predict the A(Z) exponent (on average by unity), over-predict the B_ϕ exponent (on average by a half), with q_{95} scaling the best matched on average. Hence, the conclusions of this study are based primarily on the A(Z) and B_ϕ scalings.

DISCUSSION.

The above results point to two leading A1:{v,χ} and several secondary, $\sum$= {E,H,A3,N,B2,…}:{v,χ }, energy transport mechanisms in the SOL plasmas considered. Radial transport is thus dominated by classical ion conduction, with an addition of electron conduction. The latter contains both classical and turbulent-electrostatic (resistive, ballooning, interchange) contributions. Net energy flow from the ion into the electron channels is implied, eg. A1(i):χ(e). On the particle scale, A1 involves diffusion of energy with radial steps of the ion gyro-radius occurring with i-i collision frequency, $\chi_\perp{}^i \sim \rho_i{}^2 \upsilon_{ii}$, which implies a quiescent plasma (consistent with the observed reduction in fluctuations of density and potential in the vicinity of the separatrix in H-modes [17]) of sufficient collisionality to assure several diffusive steps. The average number of diffusive steps $N_{\perp,\alpha}$, for species $\alpha \in$ {e,i}

is just the ratio of || and collisional times, $N_{\perp,\alpha} \sim \tau_{\|\alpha}/\tau_{\alpha\alpha}$, so that $N_{\perp,e} \sim L_{\|}^{2}/\chi_{\|e}\tau_e \sim \upsilon^{*}_{e}{}^{2}$ while $N_{\perp,i} \sim L_{\|}/c_s\tau_i \sim \upsilon_i$. Consequently, the diffusive approximation is valid for all but one discharge in Table 1 ($N_{\perp,e} > 30\text{-}900$, $N_{\perp,i} > 1.5\text{-}30$). Both numbers approach unity as $\upsilon^{*}_{\alpha} \rightarrow 1$ and zero as $\upsilon^{*}_{\alpha} \rightarrow 0$. In this limit, the power width should reduce to a combination of gyro-radii expressions X-Z. In fact, ion orbit loss X ~ $\rho_{\theta i}$(Y2) has been identified as the cause of deposited power profile peaking (narrow λ_q) in high power D H-modes (eg. 50397), for which $\upsilon^{*}_{i} \sim 1$ [7]. Consequently, under quiescent conditions classical ion transport reduces to IOL in the collisionless limit, A1:v$\rightarrow$X as $\upsilon^{*}_{i} \rightarrow 0$. The composite picture can be drawn as follows,

$$(\upsilon^{*}_{e} > 3, \upsilon^{*}_{i} > 3) \quad \Rightarrow \quad \text{A1:v} \quad > \quad \{\text{A1:}\chi, \Sigma\}$$
$$(\upsilon^{*}_{e} > 1, \upsilon^{*}_{i} < 1) \quad \Rightarrow \quad \text{A1:v} \rightarrow \text{X} \quad >> \quad \{\text{A1:}\chi \rightarrow 0, \Sigma\}$$

Note that ion and electron channels become de-coupled as $\upsilon^{*}_{i} < 1$, since $\upsilon^{*}_{e,i} << \upsilon^{*}_{i,i}$.

In neo-classical conduction A2 the diffusive steps take place with a poloidal gyro-radius $\rho_{\theta i}$ ~ banana width [10]. This process should be negligible in the SOL, where due to the open topology of magnetic field lines nearly all ion orbits terminate at divertor targets, precluding the existence of banana orbits for all but a small fraction of ions. In the collisionless limit, neo-classical effects appear in the SOL in the footprint of IOL X on the target, which scales as $\rho_{\theta i}$ (Y2) rather than ρ_i (Y1).

So far only the scaling of λ_q was considered. One can also compare the magnitude of predicted and measured power widths for selected models. On average, λ_q^{TC} is roughly three times smaller than $\lambda_q^{A2:v}$, two times larger than $\lambda_q^{A1:v}$ and $\rho_{\theta i}$, five times larger than λ_q^{X}, and thirty times larger than λ_q^{A3}: and $\rho_{\theta e}$. The measured widths are well matched by $\lambda_q^{TC} \sim (2.66\pm0.32)\lambda_q^{A1:v}$. Extrapolating based on this expression from JET shot 50397 to ITER using reference values for a D^+ plasma cited in [6], yields λ_q^{ITER}/~ 4±0.5 mm-omp (in general, ion widths {A1,A2,X,Y1,Y2} predict $\lambda_q^{ITER}/\lambda_q^{50397}$~0.75±0.1, while electron widths {A3,Z1,Z2} yield ~ 0.9±0.2). The same value is obtained using the regression results of Table 2, replacing $P_t \Rightarrow P_t/R^2$ and $q_{95} \Rightarrow Rq_{95}$. For a mixture of D, T and He in the ratio 5:5:1, both widths increase by ~ 15%. It is worth noting that $\lambda_q^{TC} \rightarrow \lambda_q^{X}$ as $\upsilon^{*}_{i} \rightarrow 1$ (best fit obtained as $\lambda_q^{TC} \sim (1.48\pm0.13)\lambda_q^{X}\upsilon^{*0.4}_{i}$) supporting the hypothesis that A1:v$\rightarrow$X in the collisionless limit. Since $\upsilon^{*ITER}_{i} \sim 1$, we expect a significant IOL contribution in ITER. Extrapolating the IOL expression yields $\lambda_q^{ITER} \sim 2.50.5$ mm-omp. The two mechanisms may be combined into a transitional estimate,

$$\lambda_q = \xi \, xC_{A1:v}\lambda_q^{A1:v} + (1\text{-}\xi)\lambda_q^{X}, \qquad \xi \equiv \upsilon^{*}_{i}/(1+\upsilon^{*}_{i})$$

which scales as $\lambda_q^{A1:v}$ and λ_q^{X} in the appropriate limits. This expression provides a good match to JET data with $C_{A1:v} \sim 2.8$, and predicts $\lambda_q^{ITER} \sim 3.30.5$ mm-omp, cf. the ITER design value of 5 mm-omp. Since the above estimates do not account for the increased closure (higher plasma/neutral compression) of the ITER divertor, they represent λ_q at the entrance into the divertor volume, and thus a lower limit on the deposited power width.

CONCLUSIONS.

Analysis of recent JET experiments presented in this study provides conclusive evidence for the suppression of ion turbulence in the vicinity of the separatrix in ELMy H-modes. Radial transport is dominated by classical ion conduction for $\upsilon^*_i > 3$ which reduces to ion orbit loss for $\upsilon^*_i < 1$. Based on these results, the ITER power width can be estimated as 3-4 mm-omp at the entrance into the divertor volume. The accuracy of this prediction will be improved in a future study, by including the above mechanisms in an existing edge transport code.

REFERENCES

[1]. P.C.Stangeby, The Plasma Boundary of Magnetic Fusion Devices, IoP Publishing (2000).

[2]. R.Aymar, The ITER design, Plasma Phys. Contr. Fusion, **44** (2002) 519.

[3]. ITER database, many authors, Nuclear Fusion, **39** (1999), 2423.

[4]. V.Riccardo et al., Plasma Phys. Contr. Fusion, **43** (2001), 881.

[5]. K.McCormick et al., J. Nucl. Materials, **266-269** (1999), 99.

[6]. W.Fundamenski, Plasma Phys. Contr. Fusion, **44** (2002), 761.

[7]. W.Fundamenski et al., 15th Plasma-Surface Int. Conf. (Gifu, Japan, 2002).

[8]. G.F.Matthews et al., J. Nucl. Materials, **290-293** (2001), 668.

[9]. R.D.Monk, "Langmuir Probe Measurements in the Divertor Plasma of the JET tokamak", Ph.D. Thesis, Imperial College London (1996).

[10]. K.Miyamoto, Plasma Physics for Nuclear Fusion, MIT Press (1987).

[11]. W.Fundamenski, "Tokamak Edge Plasma Modelling Using an Improved Onion-Skin Method", Ph.D. Thesis, U.Toronto (1999).

[12]. W.Fundamenski, J. Nucl. Materials, **290-293** (2001), 593.

[13]. A.Chankin, , J. Nucl. Materials, **290-293** (2001), 518.

[14]. J.W.Connor et al., Nuclear Fusion, **39** (1999), 169.

[15]. G.Councell, J. Nucl. Materials, **266-269** (1999), 91.

[16]. J.A.Heikkinen, Phys.Plasmas, **8** (2001), 2824.

[17]. J.W.Connor et al., Plasma Phys. Contr. Fusion, **42** (2000), R1.

Table 1:
Summary of selected discharges; also $L_{||}[m] \cong 50\ (q_{95}/2.6)$; $n_{i,u} = n_{e,u}/Z$; $\vartheta_u = (T_i/T_e)_u = 2$ assumed; $\nu^*_{ei} = Z\nu^*_e$

	Ions	Mode	I_p	B_ϕ	q_{95}	$\langle n_e \rangle$	P_{NB}	P_{SOL}	P_t	q_0^{TC}	q_0^{LP}	λ_q^{TC}	λ_q^{LP}	$n_{e,u}$	$T_{e,u}$	ν^*_i	ν^*_e
	>95%		MA	T		$10^{19}m^{-3}$	MW	MW	MW	MW/m^2	MW/m^2	mm	mm	$10^{19}m^{-3}$	eV		
50415	D	L	2.5	2.4	2.6	3.3	4	2.5	1.8	2.7	2.8	8.5	13	2.45	59	7.4	29
50386	D	H-I	2.5	2.4	2.6	6.0	10	6.0	4.0	7.0	3.3	7.5	8.5	1.58	77	2.7	11
50397	D	H-I	2.5	2.4	2.6	6.5	16	9.0	5.8	14	4.2	5.5	9.5	1.30	94	1.5	6
53981	He	L	2.5	2.4	2.6	3.8	2.5	2.9	2.1	1.9	1.6	14.5	14	1.12	54	32	16
53982	He	L	2.5	2.4	2.6	4.2	5.4	4.7	3.4	3.3	2.7	13.5	14.5	1.59	63	34	17
54140	He	H-III	1.5	1.45	2.6	6.1	9.2	7.0	5.35	3.8	2.7	18.5	20	1.54	65	30	15
54142	He	H-III	1.5	1.45	2.6	6.3	10.3	7.5	5.8	4.1	3.0	18.5	23.5	1.51	66	28	14
54149	He	H-III	1.5	2.2	3.8	4.7	11.5	7.2	4.1	3.1	3.3	17.5	20	1.17	68	30	15
54150	He	H-III	2.1	2.0	2.6	6.7	11.5	7.2	4.8	4.5	3.3	14	19	1.47	68	26	13

Table 2:
Regression results: exponents in $\lambda_q \propto A^\alpha Z^\beta B_\phi^{\ \gamma} q_{95}^{\ \delta} P_t^{\ \varepsilon} n_{e,u}^{\ \varphi}$.

	$\alpha+\beta$	γ	δ	ε	φ
$\lambda_{TC}^{\ selected}$	0.91±0.14	-0.99±0.27	0.71±0.25	-0.26±0.11	0.13±0.19
$\lambda_{TC}^{\ all\ D+He}$	0.94±0.08	-1.18±0.16	0.79±0.19	-0.39±0.05	0.15±0.05
$\lambda_{TC}^{\ H\text{-}mode}$	0.97±0.16	-1.17±0.28	0.69±0.27	-0.49±0.08	0.12±0.06
$\lambda_{TC}^{\ D}$	-	-	-	0.41±0.07	0.14±0.06
$\lambda_{TC}^{\ He}$	-	-1.08±0.13	0.81±0.15	-0.35±0.11	0.27±0.19
$\lambda_{LP}^{\ selected}$	0.77±0.24	-1.00±0.35	0.75±0.37	-0.16±0.13	0.54±0.36

Table 3

Theoretical scalings: exponents in $\chi_\perp \propto A^\mu Z^\eta B^\xi q_{95}{}^\zeta n_e{}^\psi T_\alpha{}^\theta \lambda_q{}^\sigma$ for models A-Q and $\lambda_q \propto A^\mu Z^\eta B^\xi q_{95}{}^\zeta n_e{}^\psi T_\alpha{}^\theta \lambda_q{}^\sigma$ for models X-Z; $n_e = Z n_i$ assumed in derivation. Primary species given in brackets. <A:Q> denotes average over models A to Q.

Model	μ	η	ξ	ζ	ψ	θ	σ
A1(i)	0.5	1	-2	0	1	-0.5	0
A2(i)	0.5	1	-2	2	1	-0.5	0
A3(e)	0	0	-2	0	1	-0.5	0
B1(i,e)	0.5	-2	-2	1	1.5	0	1
B2(i,e)	0	0	-2	1	1.5	0	1
C(i,e)	0.5	-2	-4	3	2.5	1	2
D(i,e)	0.5	-2	0	-1	0.5	-1	0
E(i,e)	0	1	-2	2	-0.5	1	1
F(i,e)	0.5	-2	-2	0.33	1.5	0	1.33
G1(i,e)	0.5	-1.5	-2	0	1	0	1
G2(e)	0.5	-0.5	-2	0.33	1.33	0	1.33
G3(i,e)	0.5	-1	-2	0	1.5	0	1
H(e)	-0.33	2.33	-2	3.33	-1.83	1.66	2.66
I(e)	0	1	0	0	-1.5	0	0
J(i,e)	-0.5	0	0	0	0.5	-1	1
K1(i,e)	0.25	-2	-2	0.5	1.5	0	1.5
K2(i,e)	0.33	-1.66	-2	0.66	0.83	0.33	1.33
L1(i,e)	0.5	-2	-2	0.33	1.5	0	1.33
L2(i,e)	0.5	-1	-2	-1	1.5	0	0
M(i)	-0.5	0	0	0	0.5	-1	0
N(e)	0	0	-1	0	1	0	0
O(i,e)	-0.5	0	0	-1	0.5	-1	0
Q(-)	0	0	0	0	0	0	0
X(i)	0.35	-0.80	-0.89	0.88	?	?	-
Y1(i)	0.5	-1	-1	0	0	0.5	-
Y2(i)	0.5	-1	-1	1	0	0.5	-
Z1(e)	0	0	-1	0	0	0.5	-
Z2(e)	0	0	-1	1	0	0.5	-
A:Q	**0.19**	**-0.52**	**-1.52**	**0.50**	**0.80**	**0.07**	**0.76**

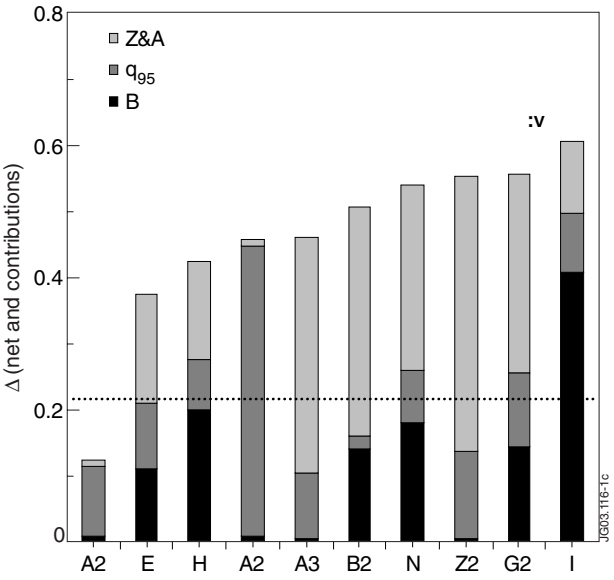

Figure 1: RMS difference Δ between the model and regression exponents, assuming ∥ convection (:v), along with contributions from Z(A), q_{95} and B_ϕ exponents. Dotted line represents RMS regression error.

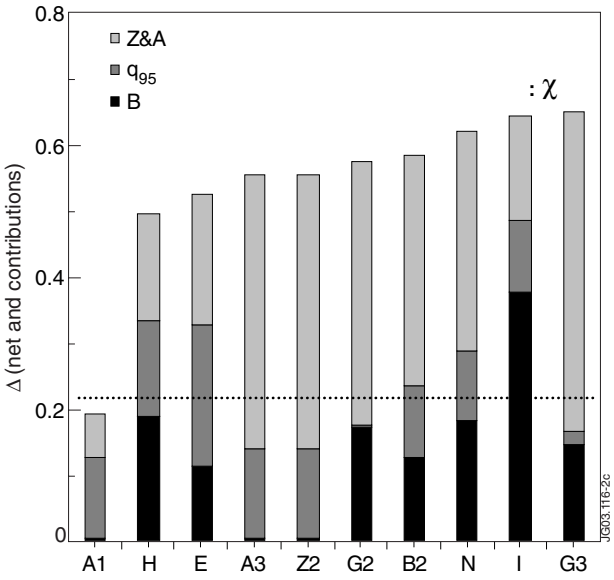

Figure 2: Same as Fig.1 but assuming ∥ conduction (:χ).